Rock and Soil Mechanics

Volume 44 | Issue 6 Article 6

10-3-2023

Three-dimensional unified mechanical model and calculation method of uplift capacity of horizontal rectangular anchor plate in the whole region in sand

Wei HU
Hunan Province Key Laboratory of Geotechnical Engineering Stability Control and Health Monitoring, Hunan University of Science and Technology, Xiangtan, Hunan 411201, China; School of Civil Engineering, Hunan University of Science and Technology, Xiangtan, Hunan 411201, China,
yilukuangben1982@163.com

Hui WANG
Hunan Province Key Laboratory of Geotechnical Engineering Stability Control and Health Monitoring, Hunan University of Science and Technology, Xiangtan, Hunan 411201, China; School of Civil Engineering, Hunan University of Science and Technology, Xiangtan, Hunan 411201, China

Chen YAO
China Railway Major Bridge Reconnaissance & Design Institute Co., Ltd. Chongqing Branch, Chongqing 400020, China

Dong-xue HAO
School of Civil Engineering and Architecture, Northeast Electric Power University, Jilin, Jilin 132012, China

See next page for additional authors

Recommended Citation

HU, Wei; WANG, Hui; YAO, Chen; HAO, Dong-xue; and SHI, Dan-da (2023) "Three-dimensional unified mechanical model and calculation method of uplift capacity of horizontal rectangular anchor plate in the whole region in sand," *Rock and Soil Mechanics*: Vol. 44: Iss. 6, Article 6.
DOI: 10.16285/j.rsm.2022.5995
Available at: https://rocksoilmech.researchcommons.org/journal/vol44/iss6/6

Three-dimensional unified mechanical model and calculation method of uplift capacity of horizontal rectangular anchor plate in the whole region in sand

Authors
Wei HU, Hui WANG, Chen YAO, Dong-xue HAO, and Dan-da SHI

Rock and Soil Mechanics 2023 44(6): 1811−1825 ISSN 1000−7598
https: //doi.org/10.16285/j.rsm.2022.5995 http://rocksoilmech.researchcommons.org/journal

Three-dimensional unified mechanical model and calculation method of uplift capacity of horizontal rectangular anchor plate in the whole region in sand

HU Wei[1, 2], WANG Hui[1, 2], YAO Chen[3], HAO Dong-xue[4], SHI Dan-da[5]

1. Hunan Province Key Laboratory of Geotechnical Engineering Stability Control and Health Monitoring, Hunan University of Science and Technology, Xiangtan, Hunan 411201, China
2. School of Civil Engineering, Hunan University of Science and Technology, Xiangtan, Hunan 411201, China
3. China Railway Major Bridge Reconnaissance & Design Institute Co., Ltd. Chongqing Branch, Chongqing 400020, China
4. School of Civil Engineering and Architecture, Northeast Electric Power University, Jilin, Jilin 132012, China
5. College of Ocean Science and Engineering, Shanghai Maritime University, Shanghai 201306, China

Abstract: Uplift of the horizontal rectangular anchor plate is a typical three-dimensional problem. However, it is difficult to characterize the sliding surface of soil around the anchor plate in the limit state for its shape is affected by a combination of the length-width ratio and embedment ratio of the anchor plate. Combining the results of ABAQUS 3D numerical simulation and 2D sliding surface analysis, it is found that the geometric form of the 3D sliding surface in any horizontal section within its buried depth range can be described by a closed graph, including four segments of straight lines parallel and equal to the long and short sides of the anchor plate respectively and four segments of 1/4 arc. The horizontal distance between the straight line and the corresponding anchor edge is determined by the 2D sliding surface in the vertical symmetric plane in the center of the long edge. The shape of this 2D sliding surface depends only on the embedment ratio, and it can be characterized by the logarithmic spiral morphological function. Based on these understandings, a three-dimensional mechanical analysis model of uplift bearing capacity of the horizontal rectangular anchor plate was constructed for the first time, and four cases of the model were analyzed. Combining the decomposition and merging of the model, the mechanical limit equilibrium analysis of the isolation body was carried out. Then, the calculation method of uplift bearing capacity of the horizontal rectangular anchor plate was deduced. It is applicable in the whole range of the length-width ratio and embedment ratio. Compared with five test cases and three other calculation methods, the results show that the proposed method has the best performance in all kinds of sand ground with various relative densities, which shows good applicability.

Keywords: rectangular anchor plate; vertical pullout; sliding surface; mechanical model; bearing capacity

1 Introduction

The mechanical analysis model of the excavated foundation of the transmission line[1], the plate and ball foundation connected by the anchor cable[2], the screw anchor pile of the photovoltaic plate structure[3], and the anchoring foundation of the marine structure[4] can be simplified as a horizontal anchor plate transferring the vertical pullout load to the surrounding soil. It relies on the pullout capacity provided by the gravity and shear strength of soil to balance the pullout load. It is called the vertical pullout problem of the horizontal anchor plate. The core is the pullout capacity analysis model and its calculation method[5−7]. At present, the research of this problem is developed generally based on the strip anchor plate which conforms to the plane strain condition[11−13] or the circular anchor plate with axisymmetric characteristics[11−13]. Murray et al.[14] stated that the length−width ratio of the strip anchor plate should be generally greater than 10 or at least 5 for the small size anchor plate, while the length−width ratio of the anchor plate used in engineering is generally not so large[15]. Therefore, it is more reasonable to regard the anchor plate used in engineering as a rectangular anchor plate except the circular anchor plate, and its three-dimensional effect is obvious, which has been confirmed by the numerical simulation results[16−18]. The theoretical analysis of the three-dimensional problem is difficult. To date, only a few scholars, such as Meyerhof[19], Zhao[20], Sahoo et al.[21], Deshmukh et al.[22] and Mokhbi et al.[23], have been involved in this research. However, Meyerhof et al.[19] did not establish a three-dimensional analysis model, but introduced the shape coefficient to consider the three-dimensional effect of the rectangular anchor plate based on the two-dimensional problem solution of the strip anchor plate. Zhao et al.[20] and Sahoo et al.[21] extended the two-dimensional analysis model constructed by Murray et al.[14] to rectangular anchor plates, where the sliding surface in the plane consisted of circular arcs at the corners and straight segments at other parts. In the model of Deshmukh et al.[22], the shape of the sliding surface in the plane was a rectangle composed of four straight

Received: 29 June 2022 Accepted: 20 October 2022
This work was supported by the National Natural Science Foundation of China (52178332, 52078108).
First author: HU Wei, male, born in 1982, PhD, Professor, PhD supervisor, research interests: ground and foundation engineering.
E-mail: yilukuangben1982@163.com

lines parallel to the length and width of the anchor plate. In the mechanical model of the square anchor plate of Mokhbi et al.[23], the sliding surface was an oblique line at the corners, as shown in Fig. 1. It can be seen that there are various assumptions about the shape of the sliding surface at the corners of the rectangular anchor plate in the plane parallel to of the anchor plate, and no corresponding construction basis is provided. The understanding is not yet unified.

In addition, the common feature of the above research results is that the sliding surface is an oblique line in the vertical plane, which is only suitable for shallow burial anchor plates. Yao et al.[10] pointed out that the current research on the anchor plate had the problem of artificially distinguishing shallow and deep burial conditions without unified criteria for the critical embedment ratio of the distinguishing index. It was emphasized that the continuous evolution of the pullout failure mechanism of the anchor plate from shallow burial to deep burial should be viewed from a unified perspective, and a morphological function that could uniformly describe the continuous evolution process of the two-dimensional sliding surface with the buried depth ratio was proposed. Then, a unified mechanical model for the vertical pullout of the strip anchor plate was constructed, and the corresponding unified calculation method of bearing capacity was derived. In this paper, the research on the three-dimensional problem of the rectangular anchor plate also starts from the viewpoint of continuous evolution of the sliding surface. First of all, the three-dimensional mechanical model of pullout capacity of the horizontal rectangular anchor plate with arbitrary embedment ratio and length−width ratio is analyzed and constructed. Then, a calculation method of bearing capacity is deduced and established. Finally, the calculation results are compared with results of test cases and other calculation methods.

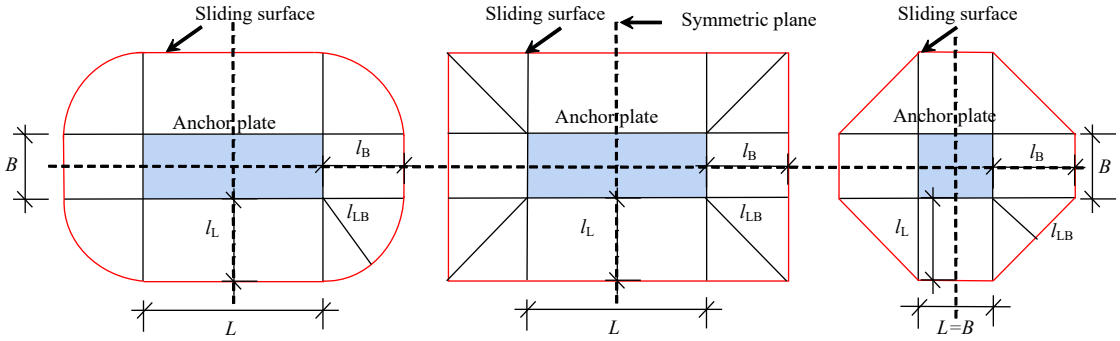

(a) Zhao's model[20] (b) Deshmukh's model[22] (c) Mokhbi's model[23]

Fig. 1 Shapes of slip surface in horizontal section

2 Unified description of sliding surface shape

According to the symmetry, in the two vertical symmetric planes of the rectangular anchor plate, the shape of the sliding surface of soil around the anchor under the limit state is the consistent with that of the sliding surface of the two-dimensional problem of the strip anchor plate. That is, the sliding surface extends to the surface in a straight or curved shape under the shallow burial condition, while it is confined to the soil interior in a "bulb" shape under the deep burial condition[24−26], as shown in Figs. 2(a) and 2(b), respectively. Within the above two-dimensional sliding surfaces, a parallel plane with distance h from the surface of the anchor plate is taken, and there are two intersection points between this plane and the sliding surfaces on the left and right sides symmetrically about the centerline of the anchor plate. Let the distance between the two intersection points and the centerline of the anchor plate be l. Then, the shape change of the sliding surface is actually a reflection of the change of l with h. For the shallow burial condition, l increases linearly with h. For the deep burial condition, the change is nonlinear and there is a certain value of h that makes the two intersection points coincide (i.e., $l = 0$). It means that the apex of the sliding surface is located below the ground surface.

For rectangular anchor plates with the same burial depth, when h is equal, due to the mutual influence between the long side and the wide side, l will have different values in other vertical planes except the vertical symmetry plane, and gradually transit from l_L in the vertical symmetry plane of the long side to l_B in the vertical symmetry plane of the wide side. In Zhao's model shown in Fig. 1(a), l_L of the long side and l_B of the wide side are equal and the corners are circular arcs (i.e., $l_{LB} = l_L = l_B$). In Deshmukh's model shown in Fig. 1(b), the shape of the sliding surface is rectangular and it also satisfies $l_L = l_B$. However, the sliding surface at the corner is bounded by 45°, which is the extension line of the long side or wide side sliding

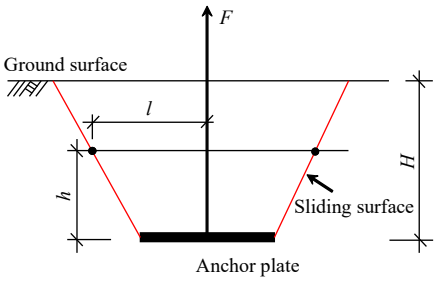

(a) Straight-line shape

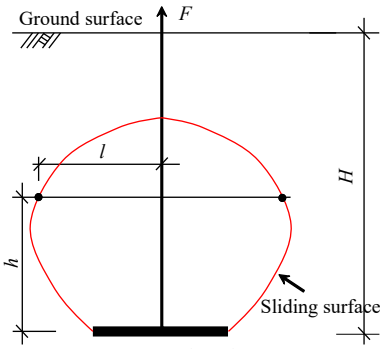

(b) "Bulb" shape

Fig. 2 Shape of slip surface in vertical section

surface. That is, l_{LB} increases from l_L to $\sqrt{2}\,l_L$ of the long side and then gradually decreases to l_B of the wide side. In Mokhbi's model shown in Fig. 1(c), it also satisfies $l_L = l_B$. However, the sliding surface at the corners are directly composed of oblique lines connecting the long side and the wide side. In contrast to Deshmukh's model, l_{LB} in the Mokhbi's model decreases from l_L to $\sqrt{2}\,l_L/2$ of the long side and then gradually increases to l_B of the wide side. Overall, there is one unified understanding among the three models. That is, l_L of the long side and l_B of the wide side are equal. However, the value and variation of l_{LB} at the corner are different among the three models. In terms of the area and perimeter enclosed by three types of sliding surfaces, Deshmukh's model is the largest, and Mokhbi's model is the smallest, and Zhao's model is the middle one. The maximum difference in the area of the corner is up to 2 times, and the maximum difference in the perimeter is up to $\sqrt{2}$ times. Since the bearing capacity of the anchor plate depends on the gravity and the shear strength of soil on the sliding surface, if the shape of the sliding surface in the vertical plane is the same, the bearing capacity of the anchor plate actually depends on the length of the sliding surface in the plane and the enclosed area. The length of the sliding surface corresponds to the bearing capacity provided by the shear strength of soil, and the area enclosed by the sliding surface corresponds to the bearing capacity provided by the gravity of soil. Therefore, the geometry of the sliding surface will have a significant impact on the calculation of the bearing capacity. However, it is obviously not fully recognized in current research results. There is no unified understanding, and the assumptions adopted are not well-founded. Therefore, in this paper, finite element software ABAQUS is used to establish the vertical pullout numerical model of horizontal rectangular anchor plates with different length−width ratios and embedment ratios. Then, the sliding surfaces of soil around the anchor in the horizontal and vertical sections under the limit state are identified, and the variations of the shape with the length−width ratio and embedment ratio are analyzed. Finally, the theoretical characterization is investigated.

3 Analysis of sliding surface shape characteristics in horizontal sections

Finite element software ABAQUS is used to establish a 1/4 three-dimensional model of uplift of the horizontal anchor plate. The material of the anchor plate is linear elastic. The elastic modulus is E_1 = 210 GPa and the Poisson's ratio is ν_1 = 0.2. The Mohr-Coulomb elastic-plastic model is used to simulate the sand. The elastic modulus E_2 ranges from 10 to 100 MPa[27]. The Poisson's ratio is ν_2 = 0.3. The internal friction angle is 20°, and the soil unit weight is γ = 17 kN/ m^3. The anchor plate−soil contact is set to hard contact with the friction coefficient f = 0.5, and the anchor plate and soil can be separated. The thickness of the anchor plate is 10 cm and the width is B = 0.4 m. Based on the definition of the strip anchor plate (length−width ratio $L/B \geqslant 10$)[14], to consider the value of the embedment ratio H/B in engineering[10] and cover shallow and deep burial conditions, L/B in this study is set to 1, 2, 3, 5 and 10 for a total of 5 conditions. H/B is set to 2, 4, 6 and 10 for a total of 4 conditions. The distances between the boundaries of the three directions of the model and the edges of the anchor plate is more than 15 times larger than the size of the anchor plate in the corresponding directions. Fixed boundary conditions is adopted and the boundary effect can be ignored[28]. The anchor plate and soil adopt the three-dimensional solid element C3D8R. A representative numerical model is shown in Fig. 3.

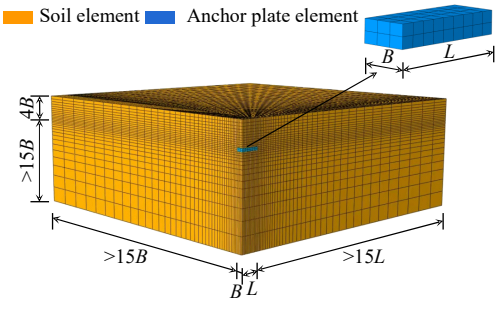

Fig. 3 Finite element numerical model (H/B = 4, L/B = 3)

The embedment ratio H/B = 4 and the aspect ratio L/B = 5 are presented as an example. The equivalent plastic strain nephograms in the planes with distances of 0.5B, B, 2B, and 3B to the upper surface of the anchor plate are extracted, and the nephogram of a representative working condition (h = B) is shown in Fig. 4. The area with the plastic deformation $\geqslant$ 0.01 is regarded as the damage region[29] (i.e., the gray area in Fig. 4). Its boundary is the sliding surface. It is found that when the elastic modulus E_2 varies within the range of 10−100 MPa, the shapes of the sliding surface are almost unaffected. The shapes of the sliding surfaces in different depth planes are similar. The length of the sliding surface and its horizontal distance to the anchor plate are proportional to the distance from the selected plane to the anchor plate. The sliding surface in the long-side direction of the anchor plate can be approximated as a straight line parallel to the long side of the anchor plate, and it starts to transit to the wide-side direction along a curve at the intersection with the extension line of the short- side projection of the anchor plate in the plane. Compared with the long side, the curved shape of the sliding surface in the wide-side direction is relatively obvious. According to the above characteristics, the sliding surface in the horizontal plane is simplified as follows. The sliding surface of the long side is taken as a straight line with a length equal to the long side of anchor plate and a horizontal distance l_L, where l_L is the horizontal distance l_{L0} from the sliding surface to the long side of the anchor plate in the symmetry plane of the long side centers of the anchor plate. The sliding surface of the wide side is taken as a straight line with a length equal to the wide side of the anchor plate and a horizontal distance l_B, where l_B is the horizontal distance l_{B0} from the sliding surface to the short side of the anchor plate in the symmetry plane of the wide side centers of the anchor plate. The sliding surface at the corner is a 1/4 arc of the ellipse with the long axis 2l_L and the short axis 2l_B, and the radius of the arc corresponding to any angle is l_{LB}, as shown in Fig. 4.

The l_{L0} and l_{B0} corresponding to the sliding surfaces in the planes under each length−width ratio and embedment ratio are extracted and calculated, and the ratio of the two are calculated as well. The variation of the ratio with the embedment ratio under different length−width ratios is shown in Fig. 5. It can be seen that the mean u of the ratio is distributed in the range of 0.9−1.1 with the maximum value 1.08, the minimum value 0.97, and the maximum standard deviation σ= 0.1. The statistical average of ratios of all data points is u = 1, and the standard deviation is σ= 0.08. It suggests that it is feasible to take l_{B0} of the wide side equal to l_{L0} of the long side. In addition, increasing the length of the anchor plate has almost no impact on the sliding surface of the wide side of the plate under the determined plate width and embedment ratio.

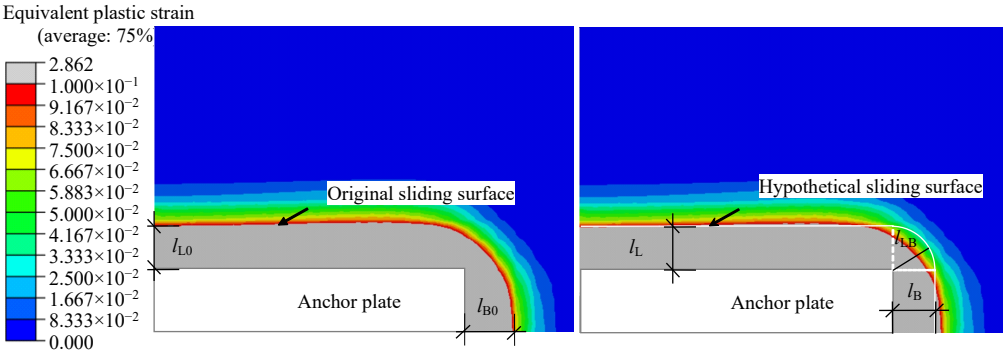

Fig. 4 Shape of sliding surface in horizontal section of h = B (H/B = 4, L/B = 5, E_2 = 30 MPa)

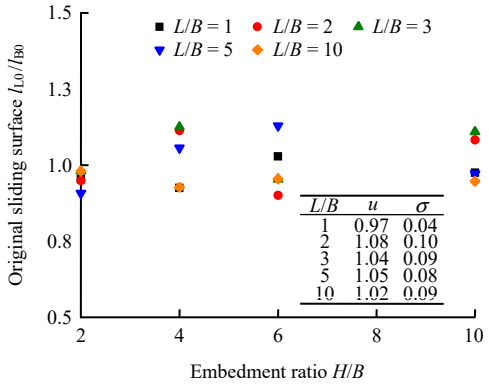

Fig. 5 Variation of l_{L0}/l_{B0} with embedment ratio

The length C_0 and the enclosed area S_0 of the original sliding surface in the plane of distance h = B to the upper surface of the anchor plate are extracted for each condition, as well as the length C_1 and the corresponding enclosed area S_1 of the hypothetical sliding surface. The ratios of C_0/C_1 and S_0/S_1 are calculated for 20 conditions, and the variations of the two with the embedment ratio are plotted in Figs. 6 and 7, respectively. For 5 conditions with different length−width ratios, the maximum and minimum values of C_0/C_1 are 1.02 and 0.96, respectively, while the maximum and minimum values of S_0/S_1 are 1.04 and 0.96, respectively.

For all working conditions, the mean and standard deviation of C_0/C_1 are u = 1.01 and σ= 0.04, respectively, while the mean and standard deviation of S_0/S_1 are u = 0.99 and σ= 0.03, respectively. It suggests that the hypothetical sliding surface is in good agreement with the actual sliding surface. Therefore, it can be used as a substitute in the theoretical analysis, which is consistent with the assumptions used in the Zhao's model.

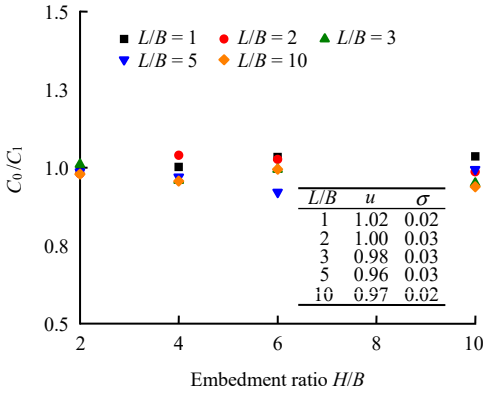

Fig. 6 Variation of C_0/C_1 with embedment ratio

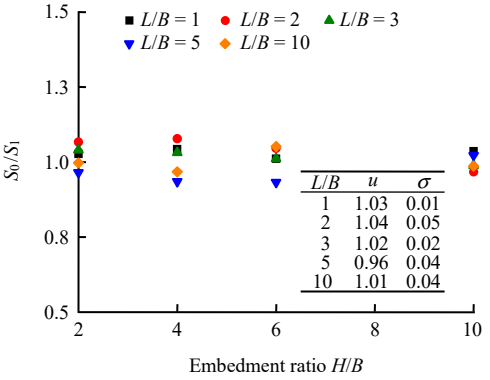

Fig. 7 Variation of S_0/S_1 with embedment ratio

Based on the calculation of l_{L0}/l_{B0}, C_0/C_1 and S_0/S_1, in the spatial sliding surface of soil around the anchor, the shape of the two-dimensional sliding surface on the horizontal section with a distance h to the surface of the anchor plate is characterized as follows. The sliding surfaces parallel to both the long side and wide side of the anchor plate are straight-line, and the horizontal distance to the corresponding side of the anchor plate is $l_L = l_B$. It is controlled by the horizontal distance l_{L0} from the sliding surface in the symmetric plane of the centers of the long sides to the centerline of the anchor plate in the horizontal section of the same depth. The value of l_{L0} is determined by the two-dimensional sliding surface established by Yao et al.[10] on uplift of the strip anchor plate. At the corner of the anchor plate, the sliding surface is 1/4 arc, and the arc radius is $l_{LB} = l_{L0} = l_{B0}$.

4 Three-dimensional unified mechanical model of rectangular anchor plate

According to the analysis in Section 3, the geometric shape of the sliding surface in the plane with a distance h to the upper surface of the anchor plate is composed of two straight lines parallel to the long side of the anchor plate, two straight lines parallel to the wide side of the anchor plate and four segments of 1/4 arcs. The horizontal distance between the sliding surface and the corresponding edge and the radius of the arc are equal to the corresponding distance of the two-dimensional sliding surface in the symmetric plane of the centers of the long sides, and they are determined by the two-dimensional sliding surface established by Yao et al.[10] on uplift of the strip anchor plate. The shape of the sliding surface changes continuously with the embedment ratio. Based on the geometry of the sliding surface in the vertical plane and the horizontal plane, a three-dimensional mechanical model of the vertical pullout capacity of the horizontal rectangular anchor plate under different burial depths can be constructed. Reference [10] divided the sliding surface into three working conditions according to the relationship between the burial depth H, the distance y_{max} from the vertex of the logarithmic spiral to the anchor plate plane and the distance y_1 from the critical point with the infinite tangent slope on the sliding surface to the anchor plate plane. In the first case, when $H < y_1$, the ground surface is lower than the critical point, and the sliding surface runs through to the ground surface. It is equivalent to the shallow burial condition. In the second case, $y_1 \leqslant H < y_{max}$. The sliding surface is inclined inwards, but it can still penetrate to the ground surface. It is equivalent to the medium burial condition. In the third case, $y_{max} \leqslant H$. The left and right sliding surfaces intersect inside the soil and no longer extend to the ground surface. They are limited to the inside of soil. It is equivalent to the deep burial condition. The three-dimensional mechanical model of the rectangular anchor plate constructed in this paper is consistent with the above two-dimensional problem when divided into different working conditions. However, the three-dimensional problem has the problem of how the long-side sliding surface and the wide-side sliding surface intersect after crossing the vertical line of the corner point, and the model before and after the intersection is different. Therefore, for the second and third working conditions, the intersection behavior at the corner should be used as a boundary to further divide the working conditions. The intersection point and the corner point are on the same vertical line. The distance to the anchor plate is set to y_3, and the corresponding polar angle is θ_3. The working conditions of the sliding surface of the three-dimensional model are divided as

follows. (1) $H<y_1$, as shown in Fig. 8(a). The ground surface is below the critical point, and the sliding surfaces on the long side, the wide side and the corner develop upwards in accordance with the sliding surface of the two-dimensional problem in their respective vertical planes. According to the previous analysis, the shape function of the sliding surface is consistent in each vertical plane. That is, D in the initial polar diameter calculation formula of the two-dimensional problem is replaced by the width B of the rectangular anchor plate. (2) $y_1 \leqslant H<y_3$, as shown in Fig. 8(b). The sliding surfaces on the long side, the wide side and the corner have passed the critical point, but have not yet intersected. (3) $y_3 \leqslant H<y_{\max}$, as shown in Fig. 8(c). The sliding surfaces have passed the intersection point, but have not been closed. The sliding surface can still extend to the ground surface. (4) $H \geqslant y_{\max}$, as shown in Fig. 8(d). The sliding surfaces are closed and confined to the interior of soil.

The three-dimensional model of each working condition can be decomposed by vertical planes corresponding to four edges of the anchor plate, the ground surface and depth planes corresponding to intersection points, and then the force and deformation analysis is carried out separately. The details are shown as follows. The spatial body of Case 1 in Fig. 8(a) can be decomposed into four 1/4 curved cones corresponding to the corner parts of the anchor plates (the four 1/4 curved cones can be combined into a complete curved cone due to the consistent geometry and force characteristics of the spatial body, as shown in Fig. 9(a)) + two curved prisms on both sides (as shown in Fig. 10(a)) + a middle curved body (as shown in Fig. 11(a)). The spatial body of Case 2 in Fig. 8(b) can be decomposed into four 1/4 curved truncated cones corresponding to the corner parts of the anchor plates (the four 1/4 curved truncated cones can be combined into a complete curved truncated cone, as shown in Fig. 9(b)) + two curved prisms on both sides (as shown in Fig. 10(b)) + a middle curved body (as shown in Fig. 11(b)). The spatial body of Case 3 in Fig. 8(c) can be decomposed into four 1/4 curved conical-cylinders corresponding to the corner parts of the anchor plates (the four 1/4 curved conical-cylinders can be combined into a complete curved conical-cylinder, as shown in Fig. 9(c)) + two curved prisms on both sides (as shown in Fig. 10(c)) + a middle curved body (as shown in Fig. 11(c)) + a upper curved truncated prism (as shown in Fig. 12(a)). The spatial body of Case 4 in Fig. 8(d) can be decomposed into four 1/4 curved cylinders corresponding to the corner parts of the anchor plates + two curved prisms on both sides (as shown in Fig. 10(c)) + a middle curved body (as shown in Fig. 11(c)) + a upper curved pyramid (as shown in Fig. 12(b)). Among them, the four 1/4 curved cylinders can be also combined into a complete curved cylinder as same as Case 3, as shown in Fig. 9(c).

After splitting and merging, each part of the isolator is subjected to the gravity G_{ij}, the resultant normal force E_{ij} and resultant shear force f_{ij} of soil on the sliding surface, and the vertical pullout load F_{ij} corresponding to this part. The subscript i represents each working condition, and its value is between 1 and 4. The subscript j represents each part of the isolator. For Cases 1 and 2, the value of j is 1−3, and for Cases 3 and 4, the value of j is 1−4. The sum of the forces of each part of the isolator under each working condition can describe the stress state of the whole isolator under the corresponding working conditions.

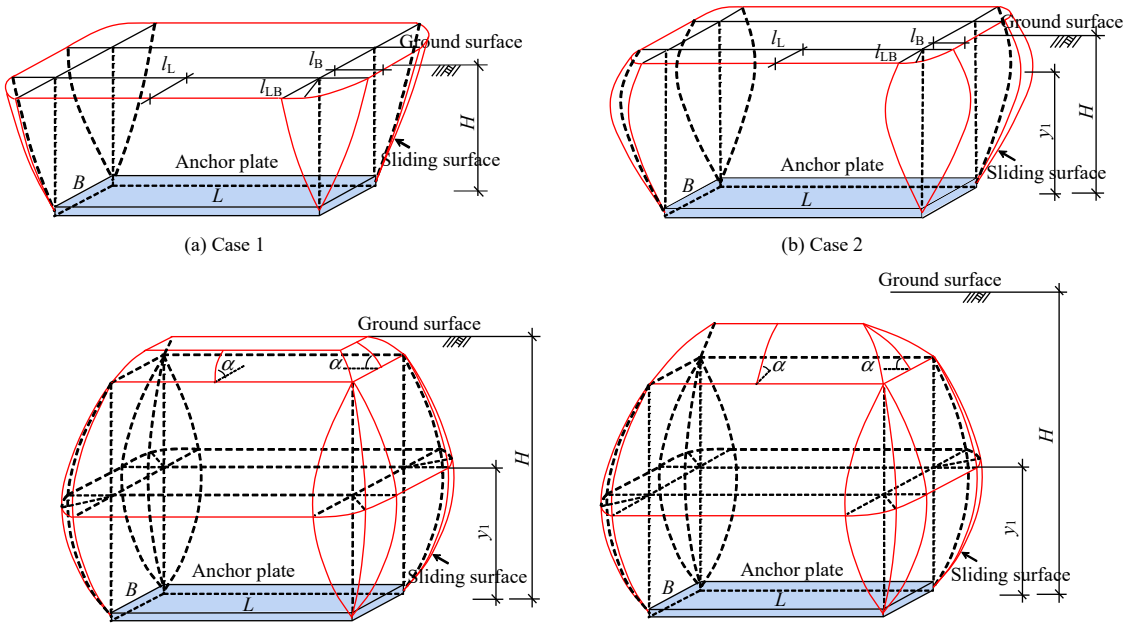

(a) Case 1 (b) Case 2

(c) Case 3 (d) Case 4

Fig. 8 Four cases of three-dimensional mechanical model

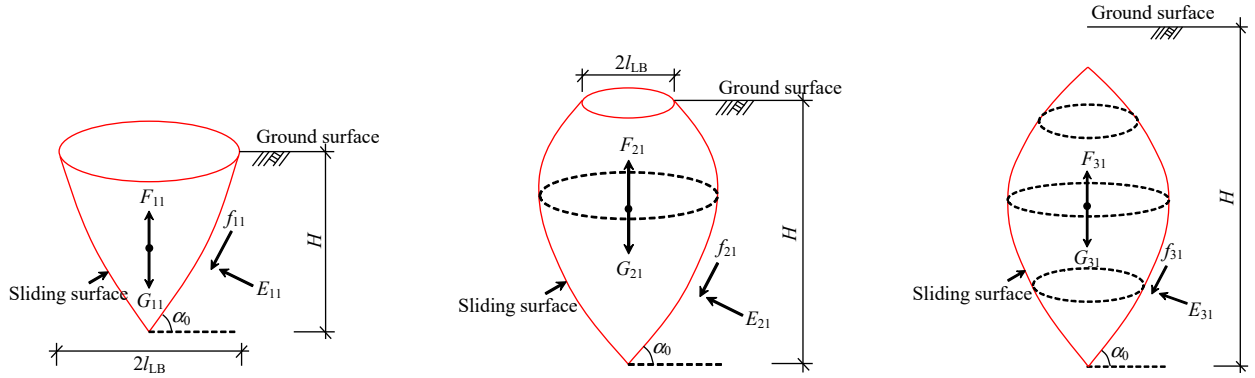

(a) Case 1 (b) Case 2 (c) Cases 3 and 4

Fig. 9 Isolator of curved cone (truncated cone, conical-cylinder)

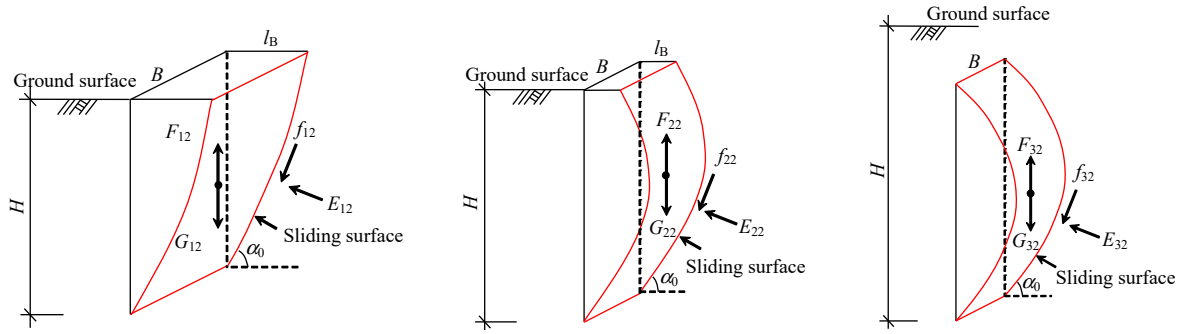

(a) Case 1 (b) Case 2 (c) Cases 3 and 4

Fig. 10 Isolator of curved prism

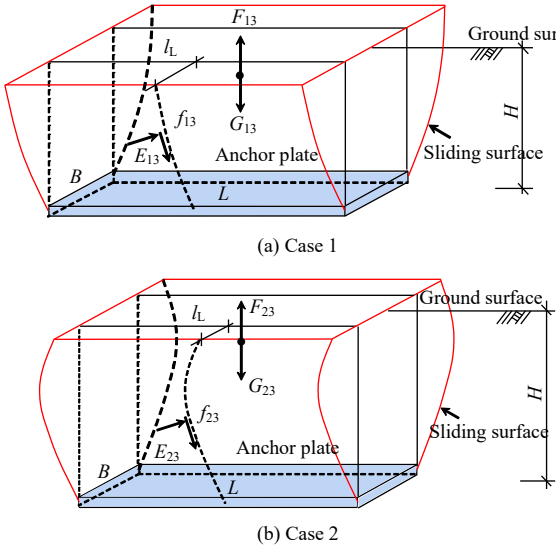

(a) Case 1

(b) Case 2

(c) Cases 3 and 4

Fig. 11 Isolator of middle curved part

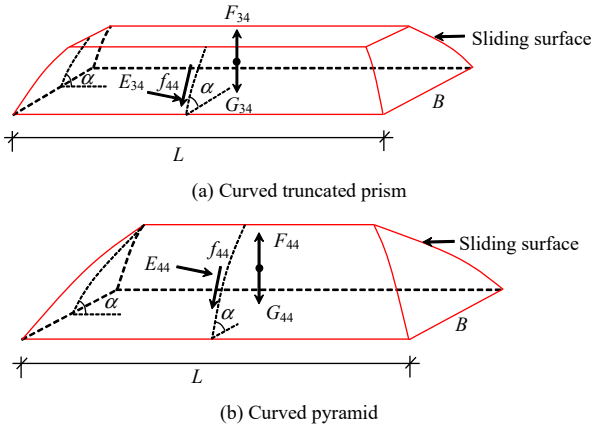

(a) Curved truncated prism

(b) Curved pyramid

Fig. 12 Isolator above the intersection

5 Unified calculation method of bearing capacity

In this paper, the shape function of the two-dimensional sliding surface in the vertical plane proposed by Yao et al.[10] is used, and the width D of the plate is replaced by the width B of the rectangular anchor plate in this paper. According to the previous analysis, the sliding surface equation is the same in the vertical plane corresponding to any point on the plate length and plate width and any rotation angle at the corner. The calculation methods of y_1, θ_1 corresponding to the critical point, θ_2 corresponding to the intersection point of the ground surface and the spiral line, and y_{max}, θ_{max} at the vertex

of the intersection of the spiral line are the same as those in Yao et al.[10]. Compared with the two-dimensional problem, the three-dimensional problem adds an intersection point when dividing the working condition, which corresponds to θ_3 and y_3. They can be obtained by Eqs. (1) and (2), respectively. The tangent slope of the sliding surface at the intersection point is determined by Eq. (3), and the corresponding tangent angle is calculated by Eq. (4).

$$\rho(\theta_3)\cos\theta_3 = r_0 \tag{1}$$

$$y_3 = r_0 e^{b\theta_3 \tan\varphi\cos\theta_3}\sin\theta_3 \tag{2}$$

$$k_1 = \frac{\rho'(\theta_3)\sin\theta_3 + \rho(\theta_3)\cos\theta_3}{\rho'(\theta_3)\cos\theta_3 - \rho(\theta_3)\sin\theta_3} \tag{3}$$

$$\alpha_1 = \arctan k_1 \tag{4}$$

According to the division of the above four working conditions, the force and deformation analysis of the corresponding isolator is carried out, and the corresponding limit equilibrium equation is established to obtain the ultimate pullout capacity of the anchor plate. For Case 1 ($H<y_1$), the overall force of the isolator is shown in Fig. 8(a). In this case, the ground surface is below the critical point, and the sliding surface penetrates to the ground surface. The curved cone, two curved prisms and the middle curved body are shown in Figs. 9(a), 10(a) and 11(a), respectively. Figs. 13(a) and 13(b) show the corresponding geometric positions of the 1/4 curved cone and the curved prism in Case 1. A micro-element is taken from the sliding surface of each part of the isolator to calculate the resultant normal force dE, the resultant shear force df and the weight dG. The integration is then performed in the interval of [0, θ_2], to find the resultant force E_{1j}, f_{1j} and G_{1j}, where j = 1, 2, 3 correspond to the three parts of the isolator. The details are shown as follows.

For the curved cone,

$$E_{11} = -\int_0^{\theta_2} 2\pi(\rho\cos\theta - r_0)\sqrt{\rho^2+\rho'^2}K_1\gamma\cdot (H-\rho\sin\theta)\cos(\arctan\lambda)\mathrm{d}\theta \tag{5}$$

$$f_{11} = \int_0^{\theta_2} 2\pi(\rho\cos\theta - r_0)\sqrt{\rho^2+\rho'^2}\gamma\tan\varphi\cdot K_1(H-\rho\sin\theta)\sin(\arctan\lambda)\mathrm{d}\theta \tag{6}$$

$$G_{11} = \int_0^{\theta_2} \pi(\rho\cos\theta - r_0)^2\gamma\rho\sin(\arctan\lambda)\mathrm{d}\theta \tag{7}$$

For the curved prism,

$$E_{12} = -2\int_0^{\theta_2} B(H-\rho\sin\theta)\sqrt{\rho^2+\rho'^2}\cdot K_1\gamma\cos(\arctan\lambda)\mathrm{d}\theta \tag{8}$$

$$f_{12} = 2\int_0^{\theta_2} B(H-\rho\sin\theta)\sqrt{\rho^2+\rho'^2}\cdot K_1\gamma\tan\varphi\sin(\arctan\lambda)\mathrm{d}\theta \tag{9}$$

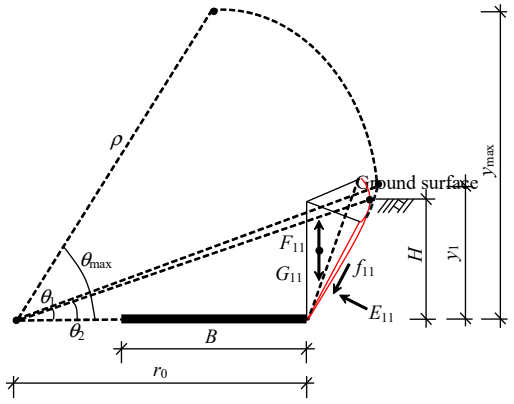

(a) 1/4 curved cone

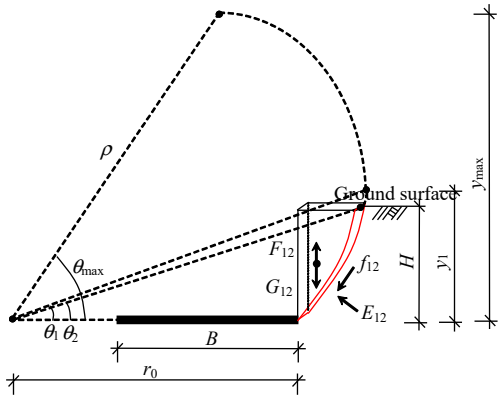

(b) Curved prism

Fig. 13 Geometric position of isolators (Case 1)

$$G_{12} = 2\int_0^{\theta_2} B\gamma(\rho\cos\theta - r_0)\rho\sin(\arctan\lambda)\mathrm{d}\theta \tag{10}$$

For the middle curved body,

$$E_{13} = -2\int_0^{\theta_2}\sqrt{\rho^2+\rho'^2}(H-\rho\sin\theta)\cdot K_1\gamma\cos(\arctan\lambda)\mathrm{d}\theta \tag{11}$$

$$f_{13} = 2\int_0^{\theta_2}\sqrt{\rho^2+\rho'^2}(H-\rho\sin\theta)K_1\cdot \gamma\tan\varphi\sin(\arctan\lambda)\mathrm{d}\theta \tag{12}$$

$$G_{13} = 2L\int_0^{\theta_2}\gamma\left[\rho\cos\theta - (r_0 - B/2)\right]\cdot (\rho'\sin\theta + \rho\cos\theta)\mathrm{d}\theta \tag{13}$$

For Case 2 ($y_1 \leqslant H < y_3$), the overall force of the isolator is shown in Fig. 8(b). In this case, the ground surface is above the critical point, but below the intersection point. The sliding surface runs through to the ground surface. After decomposition, the isolator includes one curved truncated cone, two curved prisms and one middle curved body, as shown in Figs. 9(b), 10(b) and 11(b), respectively. Figs. 14(a) and 14(b) show the geometric positions of the 1/4 curved truncated cone and the curved prism in Case 2. Similar to the calculation of Case 1, E_{2j}, f_{2j} and G_{2j} of each isolator are calculated respectively (j = 1, 2, 3). It should be noted that when the ground surface is above

the critical point, the vertical components of the resultant normal forces on the upper and lower sliding surfaces are opposite with the critical point as the boundary.

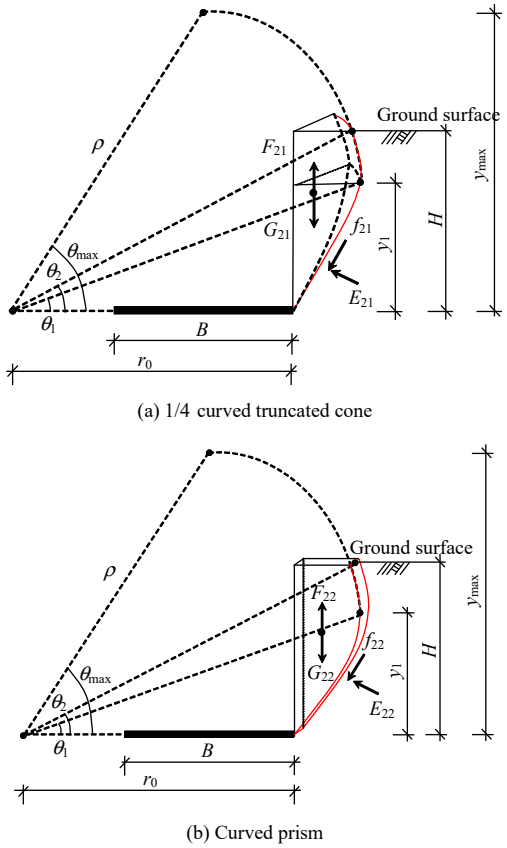

(a) 1/4 curved truncated cone

(b) Curved prism

Fig. 14 Geometric position of isolators (Case 2)

For the curved truncated cone,

$$E_{21}=-\int_0^{\theta_1}2\pi\left(\rho\cos\theta-r_0\right)\sqrt{\rho^2+\rho'^2}K_1\gamma\cdot(H-\rho\sin\theta)\cos\left(\arctan\lambda\right)\mathrm{d}\theta+\int_{\theta_1}^{\theta_2}2\pi\left(\rho\cos\theta-r_0\right)\cdot\sqrt{\rho^2+\rho'^2}K_2\gamma(H-\rho\sin\theta)\cos\left(\arctan\lambda\right)\mathrm{d}\theta \quad (14)$$

$$f_{21}=\int_0^{\theta_1}2\pi\left(\rho\cos\theta-r_0\right)\sqrt{\rho^2+\rho'^2}\gamma\tan\varphi K_1\cdot(H-\rho\sin\theta)\sin\left(\arctan\lambda\right)\mathrm{d}\theta-\int_{\theta_1}^{\theta_2}2\pi\left(\rho\cos\theta-r_0\right)\cdot\sqrt{\rho^2+\rho'^2}\gamma\tan\varphi K_2(H-\rho\sin\theta)\sin\left(\arctan\lambda\right)\mathrm{d}\theta \quad (15)$$

$$G_{21}=\int_0^{\theta_1}\pi\left(\rho\cos\theta-r_0\right)^2\gamma\rho\sin(\arctan\lambda)\mathrm{d}\theta-\int_{\theta_1}^{\theta_2}\pi\left(\rho\cos\theta-r_0\right)^2\gamma\rho\sin(\arctan\lambda)\mathrm{d}\theta \quad (16)$$

For the curved prism,

$$E_{22}=-2\int_0^{\theta_1}(H-\rho\sin\theta)\sqrt{\rho^2+\rho'^2}\cdot BK_1\gamma\cos\left(\arctan\lambda\right)\mathrm{d}\theta+2\int_{\theta_1}^{\theta_2}(H-\rho\sin\theta)\cdot\sqrt{\rho^2+\rho'^2}BK_2\gamma\cos\left(\arctan\lambda\right)\mathrm{d}\theta \quad (17)$$

$$f_{22}=2\int_0^{\theta_1}B(H-\rho\sin\theta)\sqrt{\rho^2+\rho'^2}\cdot K_1\gamma\tan\varphi\sin\left(\arctan\lambda\right)\mathrm{d}\theta-2\int_{\theta_1}^{\theta_2}B(H-\rho\sin\theta)\cdot\sqrt{\rho^2+\rho'^2}K_2\gamma\tan\varphi\sin\left(\arctan\lambda\right)\mathrm{d}\theta \quad (18)$$

$$G_{22}=2\int_0^{\theta_1}B\gamma\left(\rho\cos\theta-r_0\right)\rho\sin(\arctan\lambda)\mathrm{d}\theta-2\int_{\theta_1}^{\theta_2}B\gamma\left(\rho\cos\theta-r_0\right)\rho\sin(\arctan\lambda)\mathrm{d}\theta \quad (19)$$

For the middle curved body,

$$E_{23}=-2\int_0^{\theta_1}\sqrt{\rho^2+\rho'^2}(H-\rho\sin\theta)\cdot K_1\gamma\cos\left(\arctan\lambda\right)\mathrm{d}\theta+2\int_{\theta_1}^{\theta_2}\sqrt{\rho^2+\rho'^2}\cdot(H-\rho\sin\theta)K_2\gamma\cos\left(\arctan\lambda\right)\mathrm{d}\theta \quad (20)$$

$$f_{23}=2\int_0^{\theta_1}\sqrt{\rho^2+\rho'^2}(H-\rho\sin\theta)K_1\cdot\gamma\tan\varphi\sin\left(\arctan\lambda\right)\mathrm{d}\theta-2\int_{\theta_1}^{\theta_2}\sqrt{\rho^2+\rho'^2}\cdot(H-\rho\sin\theta)K_2\gamma\tan\varphi\sin\left(\arctan\lambda\right)\mathrm{d}\theta \quad (21)$$

$$G_{23}=2L\int_0^{\theta_1}\left[\rho\cos\theta-\left(r_0-B/2\right)\right]\rho\sin(\arctan\lambda)\mathrm{d}\theta-2L\int_{\theta_1}^{\theta_2}\left[\rho\cos\theta-\left(r_0-B/2\right)\right]\rho\sin(\arctan\lambda)\mathrm{d}\theta \quad (22)$$

For Case 3 ($y_3\leqslant H<y_{\max}$), the overall force of the isolator is shown in Fig. 8(c). In this case, the ground surface is above the intersection point, but below the vertex. The sliding surface penetrates to the ground surface. After decomposition, the isolator includes one curved conical-cylinder, two curved prisms, one middle curved body and one curved truncated prism, as shown in Figs. 9(c), 10(c), 11(c) and 12(a), respectively. For Case 4 ($H\geqslant y_{\max}$), the overall force of the isolator is shown in Fig. 8(d). In this case, the ground surface is above the vertex of the spiral line, and the sliding surface is limited to the interior of soil. After decomposition, the isolator includes one curved conical-cylinder, two curved prisms, one middle curved body and one curved pyramid, as shown in Figs. 9(c), 10(c), 11(c) and 12(b), respectively. The calculation of the two cases is only different in the fourth part (i.e., the curved truncated prism and the curved pyramid). The calculation of the corresponding quantities in the other three parts only needs to change the upper limit of the integral interval of the corresponding quantities in the Case 2 to θ_3. The geometric positions corresponding to the force calculation of the 1/4 curved cylinder and the curved prism are shown in Figs. 15(a) and 15(b), respectively. For the curved truncated prism in Case 3 and the curved pyramid in Case 4, the equations of the corresponding quantities E_{ij},f_{ij} and G_{ij} ($i=3, 4$; $j=4$) are given as follows:

$$E_{34}=2\int_{\theta_3}^{\theta_2}\frac{y_{\max}-\rho\sin\theta}{y_{\max}-y_3}(L+B)\sqrt{\rho^2+\rho'^2}K_2\cdot\gamma(H-\rho\sin\theta)\cos(\arctan\lambda)\mathrm{d}\theta \quad (23)$$

$$f_{34}=-2\int_{\theta_3}^{\theta_2}\frac{y_{\max}-\rho\sin\theta}{y_{\max}-y_3}(L+B)K_2\gamma\sqrt{\rho^2+\rho'^2}\cdot(H-\rho\sin\theta)\tan\varphi\sin(\arctan\lambda)\mathrm{d}\theta \quad (24)$$

$$G_{34}=-2\int_{\theta_3}^{\theta_2}\frac{y_{\max}-\rho\sin\theta}{y_{\max}-y_3}(L+B)\gamma\rho\sin(\arctan\lambda)\mathrm{d}\theta \quad (25)$$

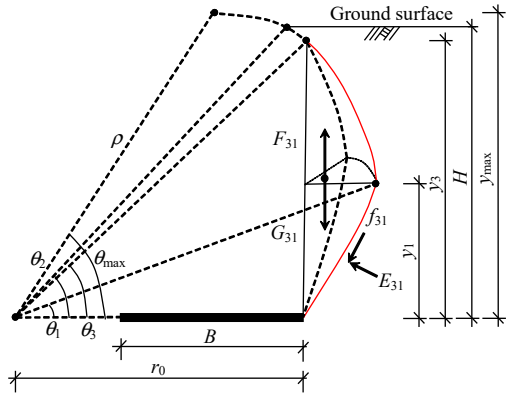

(a) 1/4 curved conical-cylinder

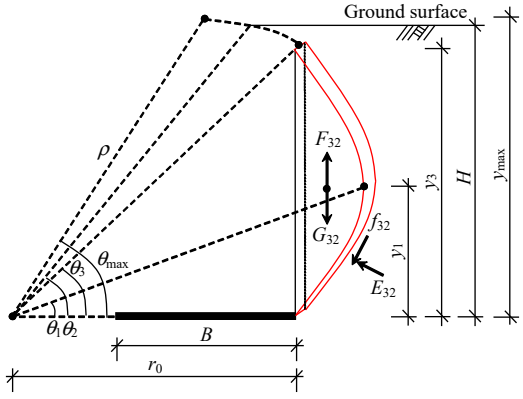

(b) Curved prism

Fig. 15 Geometric position of isolators (Cases 3 and 4)

The calculation of E_{44}, f_{44} and G_{44} corresponding to the fourth part of the isolator in Case 4 only needs to change the upper limit of the integral in the calculation formulas of E_{34}, f_{34} and G_{34} to $\theta_{\max}$.

According to the limit stress equilibrium condition of the whole isolator, the ultimate pullout capacity of the anchor plate under each working condition is calculated as follows:

$$T_{ui}=\sum_{i=1,\ j=1}^{i=4,\ j=3\text{ or }4}F_{ij}=\sum_{i=1,\ j=1}^{i=4,\ j=3\text{ or }4}(E_{ij}+f_{ij}+G_{ij}) \quad (26)$$

where i = 1, 2, 3, 4 correspond to the four cases of force calculation of the isolator, respectively; j = 1, 2, 3, 4 correspond to each decomposed part of the isolator. For Cases 1 and 2, the value of j is 1−3, and for Cases 3 and 4, the value of j is 1−4.

On the calculation of earth pressure at each point on the sliding surface, Yao et al.[10] analyzed the earth pressure behavior at the edge of the anchor plate, the critical point and the vertex of the theoretical sliding surface. They considered that the soil at the edge of the anchor plate was squeezed most strongly, assumed that this point was subjected to the passive earth pressure, and took the Rankine passive earth pressure coefficient K_p. The sliding surface moved upward relative to the outer soil at the critical point. Assuming that this point was subjected to the static earth pressure, the static earth pressure coefficient $K_0=1-\sin\varphi$ was taken. The earth pressure coefficient at the vertex of the theoretical sliding surface was taken as 1, and the earth pressure coefficients K_1 and K_2 of the remaining points were calculated by linear interpolation between the above earth pressure coefficients according to the vertical distance from each point to the anchor plate. We believe that the above-mentioned values of the earth pressure coefficients at the edge of the anchor plate and the vertex of the theoretical sliding surface are debatable, as shown in Fig. 16.

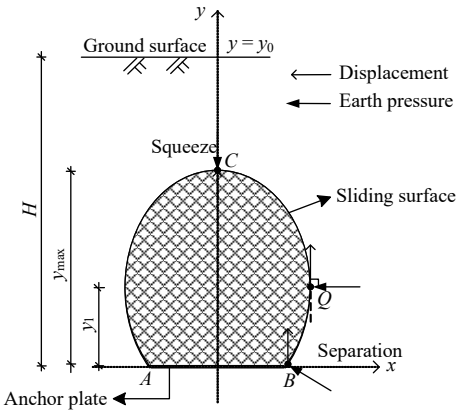

Fig. 16 Analysis of earth pressure coefficient

Although the anchor plate squeezes the soil most strongly at point B of the edge, this is for the soil inside the sliding surface, and the earth pressure acting on the sliding surface comes from the external soil. The soil inside the sliding surface has an upward displacement at this point relative to the external soil, and the two tend to separate from each other. Therefore, the earth pressure tends to be active earth pressure, and the active earth pressure coefficient $K_a=\tan^2(\pi/4-\varphi/2)$ is used. At point C of the vertex of the theoretical sliding surface, the outer soil is squeezed by the soil inside the sliding surface, and the soil is in a state of failure. Therefore, the earth pressure at this point should be passive earth pressure and $K_p=$

$\tan^2(\pi/4+\varphi/2)$. The critical point is still the coefficient of earth pressure at rest $K_0=1-\sin\varphi$. The calculation of soil pressure coefficients K_1 and K_2 at other points still adopts the following linear interpolation calculation method:

$$K_1 = K_a + (K_0 - K_a)\rho\sin\theta / y_1 \quad (27)$$

$$K_2 = K_p - \frac{K_p - K_0}{y_{max} - y_1}(\rho\sin\theta - y_1) \quad (28)$$

6 Comparison and verification

6.1 Test cases and calculation method

To verify the validity of the calculation method of bearing capacity in this paper, three other calculation methods and five test cases are introduced for comparison and verification. The three calculation methods are described as follows. (1) Murray et al.[14] method, denoted as Method 1: It is proposed based on a straight-line failure plane at the edge of the plate and a portion of a circular cone at corners. (2) Frydman et al.[30] method, denoted as Method 2: It introduces a shape factor based on the calculation method of the bearing capacity of the strip anchor plate. The shape factor is obtained by fitting the experimental results. (3) Deshmukh et al.[22] method, denoted as Method 3: In the analysis model of this method, the sliding surface in the vertical plane is also straight-line, but the corners are rectangular. (4) The method in this paper, denoted as Method 4: It works according to Eq. (26). All the parameters involved are consistent with those by Yao et al.[10], such as the initial angle of sliding surface α_0, constant a, etc. For loose sand (relative density $D_r<0.33$)[31], $\alpha_0=\pi/2-\varphi/2$. For medium sand (relative density $0.33\leqslant D_r\leqslant 0.67$)[31], $\alpha_0=\pi/2-3\varphi/4$. For dense sand (relative density $D_r>0.67$)[31], $\alpha_0=\pi/2-\varphi$. The constant a is taken as 0.01, 0.02 and 0.03 respectively for loose, medium and dense sand. The internal friction angle is taken as the peak internal friction angle.

Five test cases include Gui[32] test (Test 1), Ding et al.[15] test (Test 2), Yao[33] test (Test 3), Rowe et al.[34] test (Test 4) and Murray et al.[14] test (Test 5). Sand is used in all tests, and the specific parameters are shown in Table 1.

It should be noted that the test curves of Gui[32], Ding[15], Murray[14] and Rowe[34] all exhibit a hardening type, and the maximum load is taken as the ultimate pullout capacity. The test curve of Yao[33] is a softening type and has a peak value. By combining the measured displacement and referring to the ultimate vertical displacement value standard[35] specified in relevant codes and the determination method of the internal friction angle previously mentioned, it is more reasonable to take the peak load as the ultimate pullout capacity. In addition, although the finite element numerical simulation is carried out in this paper, the main purpose is to identify the shape of the sliding surface under the limit state, and the finite element calculation results of the pullout capacity are not extracted and compared with the theoretical calculation results. The reasons are analyzed as follows. The previous numerical simulation results show that the elastic modulus of soil will not affect the shape of the sliding surface. However, the sliding surface is defined by the size of plastic deformation ($\geqslant$ 0.01). The greater the elastic modulus of soil, the greater the load required to achieve the same size of plastic deformation. If only the elastic modulus is changed and the internal friction angle of soil keeps constant in the numerical simulation, the calculated value of the pullout capacity of the anchor plate will be significantly affected by the value of the elastic modulus of soil. However, when the confining pressure is the same, the greater the internal friction angle of sand, the greater the elastic modulus of sand. That is, the elastic modulus of sand is related to the internal friction angle, but the relationship between the two is unknown. Meanwhile, the theoretical calculation method does not involve this parameter, and the test case does not provide its value. All of them only reflect the influence of soil properties by the internal friction angle of the strength index. In this case, the pullout capacity calculated by artificially setting the elastic modulus in the numerical simulation will be unreliable, and it is not of practical significance to be compared with the theoretical value.

Table 1 Basic parameters of the test cases

Test No.	Internal friction angle φ/(°)	Unit weight γ/(kN • m^{-3})	Sand property	Width of anchor plate B /m	Length-width ratio L/B	Embedment ratio H/B
Test 1	37.8	15.50	Dense sand	0.100 0	1	1, 2, 3, 4, 5, 6
Test 2	32.2	14.11	Loose sand	0.050 0	1	2, 3, 4, 5, 6, 7, 8
	45.0	15.91	Dense sand			2, 3, 4, 5, 6, 7, 8
Test 3	33.1	16.98	Medium sand	0.075 0	1	1, 2, 4, 8
				0.075 0	5	
Test 4	32.0	14.99, 14.15	Medium sand	0.051 0	1	3
		14.80, 15.04			2	3
		14.99, 15.15			3	3
		14.77−15.00			5	3, 6, 8
Test 5	44.0	16.80±0.20	Dense sand	0.050 8	1	1, 2, 3, 4, 6, 8, 10
					3	1, 2, 3, 4, 6, 8, 10
					5	1, 2, 3, 4

6.2 Comparative analysis of results

The above three methods and the method in this paper are used to calculate the test cases. The ratio F_s is defined as the ratio of the calculated value T_u of the pullout capacity to the test value T_m. The closer F_s is to 1, the better the

calculation effect is. The test value T_m and the calculated value T_u of each method are compared as shown in Table 2. The ratio T_u/T_m is also calculated in the table and statistically analyzed. The corresponding mean u and standard deviation σ are calculated and used as indicators to compare the calculation effect of each method. The comparison process consists of three steps:

(1) First, calculate the means u_A and u_B of ratio F_s of Method A and Method B. If $|u_A-1|-|u_B-1|\geqslant 0.1$, then Method B is better than Method A. If $|u_B-1|-|u_A-1|\geqslant 0.1$, the calculation effect of Method A is better than that of Method B. If both conditions are not valid, the next step is performed.

(2) Two cases are divided in this step. i) If u_A and

Table 2 Comparison of calculated value T_u and measured value T_m

Test No.	L/B	H/B	Sand property	T_m	Method 1		Method 2		Method 3		Method 4	
					T_u	T_u/T_m	T_u	T_u/T_m	T_u	T_u/T_m	T_u	T_u/T_m
Test 1	1	1	Dense sand	37.50	28.02	0.75	41.56	1.11	26.11	0.70	45.26	1.21
		2		125.00	88.68	0.71	175.38	1.40	73.45	0.59	156.95	1.26
		3		200.00	193.40	0.97	407.07	2.04	142.02	0.71	220.22	1.10
		4		275.00	353.59	1.29	743.99	2.71	231.82	0.84	372.39	1.35
		5		375.00	580.68	1.55	1 191.91	3.18	342.84	0.91	531.09	1.42
		6		475.00	886.07	1.87	1 755.56	3.70	475.09	1.00	668.17	1.41
Test 2	1	2	Loose sand	12.42	8.83	0.71	17.67	1.42	7.60	0.61	12.59	1.01
		3		28.49	18.61	0.65	40.22	1.41	14.45	0.51	24.20	0.85
		4		45.99	33.19	0.72	72.61	1.58	23.35	0.51	37.20	0.81
		5		68.67	53.51	0.78	115.34	1.68	34.27	0.50	56.54	0.82
		6		90.91	80.47	0.89	168.83	1.86	47.24	0.52	84.33	0.93
		7		107.54	115.01	1.07	233.43	2.17	62.24	0.58	104.51	0.97
		8		126.57	158.06	1.25	309.45	2.44	79.27	0.63	153.19	1.21
Test 3	1	2	Dense sand	31.16	15.96	0.51	31.45	1.01	12.56	0.40	32.52	1.04
		3		74.42	36.18	0.49	74.63	1.00	24.72	0.33	71.18	0.96
		4		157.93	67.97	0.43	138.27	0.88	40.79	0.26	134.30	0.85
		5		288.95	113.86	0.39	223.56	0.77	60.77	0.21	220.71	0.76
		6		462.07	176.41	0.38	331.45	0.72	84.68	0.18	423.50	0.92
		7		690.25	258.17	0.37	462.76	0.67	112.50	0.16	652.30	0.95
		8		1 048.31	361.68	0.35	618.17	0.59	144.23	0.14	973.50	0.93
	1	1	Medium sand	18.70	12.08	0.65	17.87	0.96	11.42	0.61	18.91	1.01
		2		48.20	36.66	0.76	73.19	1.52	31.36	0.65	54.72	1.14
		4		179.00	139.17	0.78	302.34	1.69	96.77	0.54	193.65	1.08
		8		326.50	668.95	2.05	1 293.72	3.96	329.78	1.01	350.07	1.07
	5	1		59.00	49.25	0.83	60.94	1.03	57.10	0.97	69.13	1.17
		2		149.40	128.02	0.86	176.85	1.18	156.78	1.05	175.91	1.18
		4		459.70	390.02	0.85	575.37	1.25	483.86	1.05	498.55	1.08
		8		3 214.00	1 443.13	0.45	2 056.62	0.64	1 648.91	0.51	2 824.37	0.88
Test 4	1	3	Medium sand	33.03	20.85	0.63	45.12	1.37	16.23	0.49	29.99	0.91
		3		33.03	21.07	0.64	45.60	1.38	16.40	0.50	41.70	1.26
	2	3		37.98	31.54	0.83	56.61	1.49	32.05	0.84	44.13	1.16
		3		41.62	32.05	0.77	57.52	1.38	32.57	0.78	45.47	1.09
	3	3		54.62	43.04	0.79	69.54	1.27	48.69	0.89	66.62	1.22
		3		57.74	43.50	0.75	70.29	1.22	49.21	0.85	56.85	0.98
		3		81.61	65.24	0.80	93.97	1.15	81.14	0.99	82.52	1.01
	5	3		82.91	65.28	0.79	94.03	1.13	81.20	0.98	82.58	1.00
		6		304.42	216.57	0.71	317.55	1.04	261.03	0.86	210.55	0.69
		8		483.48	380.99	0.79	543.67	1.12	438.52	0.91	411.30	0.85
		8		488.37	381.25	0.78	544.04	1.11	438.82	0.90	452.17	0.93
Test 5	1	1	Dense sand	5.32	8.61	1.62	6.54	1.23	3.98	0.75	5.77	1.08
		2		21.30	38.63	1.81	28.63	1.34	11.52	0.54	25.64	1.20
		3		74.59	102.96	1.38	67.75	0.91	22.62	0.30	61.56	0.83
		4		137.53	214.52	1.56	125.30	0.91	37.28	0.27	112.53	0.82
		6		445.98	630.92	1.41	299.75	0.67	77.28	0.17	338.27	0.76
		8		964.46	1 391.07	1.44	558.42	0.58	131.52	0.14	891.34	0.92
		10		1 782.98	2 598.21	1.46	905.98	0.51	199.99	0.11	1 343.81	0.75
	3	1		6.46	12.94	2.00	10.48	1.62	7.96	1.23	6.86	1.06
		2		25.84	51.54	1.99	38.77	1.50	23.05	0.89	34.27	1.33
		3		77.06	128.71	1.67	86.09	1.12	45.25	0.59	78.14	1.01
		4		145.30	257.36	1.77	153.59	1.06	74.57	0.51	139.03	0.96
		6		446.28	720.71	1.61	352.48	0.79	154.57	0.35	510.87	1.14
		8		1 008.31	1 544.81	1.53	640.74	0.64	263.04	0.26	1 093.87	1.08
		10		1 818.78	2 832.92	1.56	1 022.23	0.56	399.98	0.22	1 567.48	0.86
	5	1		20.86	27.20	1.30	22.30	1.07	19.91	0.95	18.14	0.87
		2		73.94	90.28	1.22	69.18	0.94	57.62	0.78	61.61	0.83
		3		162.41	212.32	1.31	141.10	0.87	113.12	0.70	130.66	0.80
		4		294.71	383.44	1.30	238.45	0.81	186.42	0.63	222.94	0.76

u_B are both less than 1 or greater than 1, calculate and define the coefficient of variation $CV_A = \sigma_A/u_A$ and $CV_B = \sigma_B/u_B$, where σ_A and σ_B are the corresponding standard deviations of Method A and Method B, respectively. If $CV_A < CV_B$, Method A is better than Method B. Otherwise, Method B is better than Method A. ii) If one of u_A and u_B is greater than 1 and the other is less than 1, then calculate and define the coefficient of variation $CV_A = \sigma_A/|u_A-1|$ and $CV_B = \sigma_B/|u_B-1|$. If $CV_A < CV_B$, Method B is better than Method A. Otherwise, Method A is better than Method B.

(3) When $u_A = u_B$ and $\sigma_A = \sigma_B$, the calculation effects of the two methods are the same.

The calculated value T_u and the test value T_m are shown in Fig. 17 under different compaction states. Different methods are distinguished by different colors, and different test conditions are distinguished by different symbols. The results of the loose sand condition is shown in Fig. 17(a). On the whole, the calculated values of Method 2 are large, and the results of the other three methods are small. The mean value of F_s in Method 2 is 1.8, which indicates that the calculated values are significantly large. It tends to increase with the increase of the embedment ratio. The mean value of F_s in Method 3 is 0.55, which indicates the calculated values are significantly small. However, its standard deviation $\sigma = 0.05$ is the smallest. It indicates that its calculation stability is good. Both Method 1 and the method in this paper are about 10% smaller, and for the method in this paper, $F_s = 0.94$ is closer to 1. According to the above evaluation method of the calculation effect, $|u_1-1|-|u_4-1| = 0.12-0.06 = 0.06$, and the second step is needed. u_1 and u_4 are both less than 1. Then the coefficients of variation are calculated as $CV_1 = \sigma_1/u_1 = 0.2/0.88 = 0.23$ and $CV_4 = \sigma_4/u_4 = 0.13/0.94 = 0.14$. Since $CV_4 < CV_1$, then the method in this paper is better than Method 1.

The calculation of the medium sand condition is shown in Fig. 17(b). In terms of the mean value of F_s, the calculated values of Method 2 and the method in this paper are large. The former is more than 60% larger, and the calculation effect is poor. The calculated values of Method 1 and Method 3 are small, and the mean values are similar. According to the above evaluation method of the calculation effect, $CV_3 = 0.24 < CV_1 = 0.39$. Therefore, the calculation effect of Method 3 is better than that of Method 1. The comparison between Method 3 and the method in this paper needs to follow the second condition of the second step of the evaluation method. $CV_3 = \sigma_3/|u_3-1| = 0.2/|0.81-1| = 1.05$ and $CV_4 = \sigma_4/|u_4-1| = 0.14/|1.04-1| = 3.5$. Since $CV_3 < CV_4$, then the method in this paper is better than Method 3.

The calculation results of the dense sand condition is shown in Fig. 17(c). The mean value of F_s of the method in this paper is 1.01, which is the closest to 1, and the standard deviation is also the smallest. There is no doubt that the calculation effect of the method in this paper is the best. The calculated values of Method 3 are about 50% smaller than the actual value. The mean values of F_s in Method 1 and Method 2 are close, and the calculated values are about 25% larger. After further evaluation, $CV_1 = \sigma_1/u_1 = 0.5/1.25 = 0.39$ and $CV_2 = \sigma_2/u_2 = 0.77/1.23 = 0.63$. Since $CV_1 < CV_2$, then Method 1 is obviously better than Method 2.

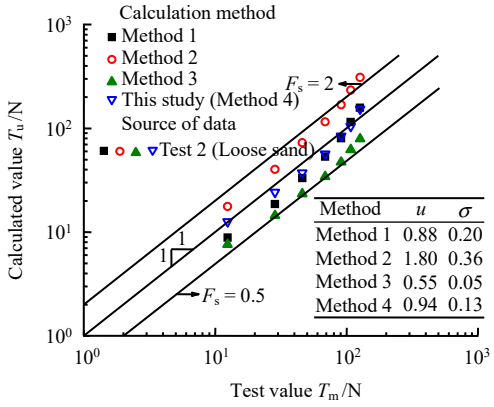

(a) Loose sand condition

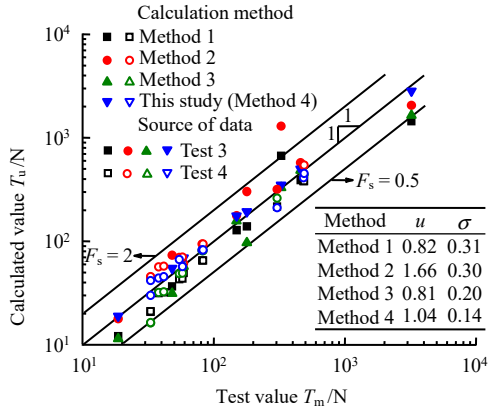

(b) Medium sand condition

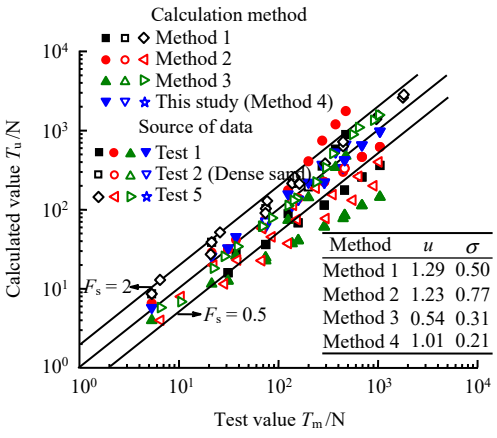

(c) Dense sand condition

Fig. 17 Comparison of calculated and measured values

7 Conclusions

For the three-dimensional behavior of the vertical pullout problem of the horizontal rectangular anchor plate, the numerical simulation method is used to analyze the shape characteristics of the spatial sliding surface of soil around the anchor in the horizontal section. The construction of the three-dimensional mechanical analysis model of uplift of the horizontal rectangular anchor plate and the derivation of the calculation method of the bearing capacity are carried out in combination with our previous theoretical study of the continuous evolution of the two-dimensional sliding surface with the embedment ratio. The main conclusions can be drawn as follows:

(1) The geometric shape of the spatial sliding surface in any horizontal section within its range can be described by four straight lines parallel to the long and short sides of the anchor plate and four 1/4 arcs. The horizontal distances between the straight lines and the corresponding anchor edges are equal, and the distance is controlled by the two-dimensional sliding surface in the vertical symmetric plane of the center of the long edge.

(2) The continuous evolution of the vertical two-dimensional sliding surface shape with the embedment ratio is characterized by the logarithmic spiral function. With the increase of the embedment ratio, the polar diameter of the spiral line decreases. It depicts the whole evolution process of the sliding surface in the vertical plane from the approximate straight line of shallow burial extending to the ground surface to the “bulb” shape of deep burial limited to the interior of soil. The whole picture of the three-dimensional sliding surface of the rectangular anchor plate is depicted by combining the characteristics of the sliding surface in the horizontal section.

(3) According to the position relationship between the burial depth of the anchor plate and the critical point, intersection point and vertex of sliding surface, the burial depth of the anchor plate can be divided into four continuous working conditions. A three-dimensional mechanical analysis model of pullout capacity of the rectangular anchor plate under each working condition is established. After decomposition and mergence of the isolator, the mechanical limit equilibrium analysis of each sub-isolation body is carried out, and the calculation method of pullout capacity of the horizontal rectangular anchor plate is established. The proposed method is applicable to rectangular anchor plates with arbitrary length−width ratio and embedment ratio.

(4) In the comparative analysis with five test cases and three calculation methods, the calculation method of pullout capacity of the horizontal anchor plate established in this paper has achieved the best calculation results in three types of sand conditions. It suggests that the proposed method has good applicability.

References

[1] HAO Dong-xue, LIU Zhu-jiang, CHEN Rong, et al. Centrifuge model test study on bearing capacity of excavated foundations of transmission lines[J]. Chinese Journal of Rock Mechanics and Engineering, 2020, 39(9): 1921−1929.

[2] WANG Xue-jiao, YAN Zhi-xin, LONG Zhe. Vertical uplift resistance of the foundation of plate and ball connected by anchor cable and its influencing factors[J]. Journal of Civil and Enviromental Engineering, 2019, 41(4): 36−43.

[3] HU Wei, MENG Jian-wei, LIU Shun-kai, et al. Experimental and theoretical researches on horizontal bearing mechanism of single screw anchor pile[J]. Chinese Journal of Geotechnical Engineering, 2020, 42(1): 158−167.

[4] HAN Cong-cong, SHEN Kan-min, LI Wei, et al. Field tests on installation performance of a new hybrid dynamically installed anchor[J]. Chinese Journal of Geotechnical Engineering, 2021, 43(9): 1657−1665.

[5] HUANG Mao-song, YU Sheng-bing. Pull-out capacity of strip anchor plate in sand based on block set mechanism[J]. Chinese Journal of Geotechnical Engineering, 2013, 35(2): 201−207.

[6] HU S, ZHAO L, TAN Y, et al. Variation analysis of uplift bearing characteristics of strip anchor plate in nonhomogeneous materials[J]. International Journal of Geomechanics, 2021, 21(4): 04021037.

[7] WANG Hong-tao, LI Shu-cai, WANG Qi, et al. Limit analysis of ultimate capacity of shallow horizontal strip anchor plate based on nonlinear failure criterion[J]. Engineering Mechanics, 2014, 31(2): 131−138.

[8] BHATTACHARYA P. Undrained uplift capacity of strip plate anchor nearby clayey slope[J]. Geotechnical and Geological Engineering, 2018, 36(2): 1393−1407.

[9] GHORAI B, CHATTERJEE S. Effect of keying –induced soil remolding on the ultimate pull-out capacity and embedment loss of strip anchors in clay[J]. Journal of Geotechnical and Geoenvironmental Engineering, 2021, 147(10). DOI: 10.1061/(ASCE)GT.1943-5606. 0002623.

[10] YAO Chen, HU Wei, MENG Jian-wei, et al. Unified method

for calculation of vertical pulling capacity of horizontal strip anchor plate in sand[J]. Engineering Mechanics, 2021, 38(5): 209−218.

[11] SHI Dan-da, MAO Yi-yao, YANG Yong, et al. Experimental study on the deformation characteristics of soils around uplift circular plate anchors using digital image correlation technology[J]. Rock and Soil Mechanics, 2020, 41(10): 3201− 3213.

[12] HU Wei, MENG Jian-wei, YAO Chen, et al. A method for calculating vertical pullout ultimate bearing capacity of shallow circular anchor plate[J]. Rock and Soil Mechanics, 2020, 41(9): 3049−3055.

[13] SRINIVASAN V, GHOSH P, SANTHOSHKUMAR G. Experimental and numerical analysis of interacting circular plate anchors embedded in homogeneous and layered cohesionless soil[J]. International Journal of Civil Engineering, 2020, 18(2): 231−244.

[14] MURRAY E J, GEDDES J D. Uplift of anchor plates in sand[J]. Journal of Geotechnical Engineering, 1987, 113(3): 202−215.

[15] DING Pei-min, XIAO Zhi-bin, ZHANG Qi-lin, et al. Uplift capacity of anchor plates in sand[J]. Journal of Building Structures, 2003, 24(5): 82−91, 97.

[16] CHOUDHARY A K, PANDIT B, BABU G. Three-dimensional analysis of uplift behaviour of square horizontal anchor plate in frictional soil[J]. International Journal of Geosynthetics and Ground Engineering, 2018, 4(2): 14.1−14.9.

[17] ROKONUZZAMAN M, SAKAI T. Evaluation of shape effects for rectangular anchors in dense sand: model tests and 3D finite-element analysis[J]. International Journal of Geomechanics, 2012, 12(2): 176−181.

[18] MERIFIELD R S. Numerical modelling of soil anchors[D]. Newcastle: University of Newcastle, 2002.

[19] MEYERHOF G G, ADAMS J I. The ultimate uplift capacity of foundation[J]. Canadian Geotechnical Journal, 1968, 5(4): 225−244.

[20] ZHAO Lian-heng, LUO Qiang, LI Liang, et al. Ultimate pullout capacity of horizontal rectangular plate anchors[J]. Chinese Journal of Geotechnical Engineering, 2009, 31(9): 1414−1420.

[21] SAHOO J P, GANESH R. Vertical uplift resistance of rectangular plate anchors in two layered sand[J]. Ocean Engineering, 2018, 150: 167−175.

[22] DESHMUKH V B, DEWAIKAR D M, CHOUDHURY D. Analysis of rectangular and square anchors in cohesionless soil[J]. International Journal of Geotechnical Engineering, 2010, 4(1): 79−87.

[23] MOKHBI H, MELLAS M, MABROUKI A, et al. Three-dimensional numerical and analytical study of horizontal group of square anchor plates in sand[J]. Acta Geotechnica, 2018, 13: 159−174.

[24] CAÑIZAL F, CASTRO J, CAÑIZAL J, et al. Pull-out capacity and failure mechanisms of strip anchors in clay[J]. Energies, 2020, 13(15): 3853.

[25] YANG M, AI Z, DENG B. Experimental and analytical study on uplift loading capacity of strip plate anchors near sand slope[J]. International Journal of Geomechanics, 2020, 20(1): 04019136.

[26] ISLAM M S, SARKAR G, TAJNIN M R, et al. Limit load of strip anchors in uniform cohesive-frictional soil[J]. Ocean Engineering, 2019, 190(C): 106428.

[27] LAI Qiong-hua. Determination of deformation moduli for rock and soil[J]. Chinese Journal of Rock Mechanics and Engineering, 2001, 20(Suppl.1): 1750−1754.

[28] ZHU Bin, XIONG Gen, LIU Jin-chao, et al. Centrifuge modelling of a large-diameter single pile under lateral loads in sand[J]. Chinese Journal of Geotechnical Engineering, 2013, 35(10): 1807−1815.

[29] GU Xiao-qiang, WU Rui-tuo, LIANG Fa-yun, et al. On HSS model parameters for Shanghai soils with engineering verification[J]. Rock and Soil Mechanics, 2021, 42(3): 833−845.

[30] FRYDMAN S, SHAHAM I. Pullout capacity of slab anchors in sand[J]. Canadian Geotechnical Journal, 1989, 26(3): 385−400.

[31] LI Guang-xin, ZHANG Bing-yin, YU Yu-zhen. Soil mechanics[M]. 2nd ed. Beijing: Tsinghua University Press, 2004.

[32] GUI Mei-bing. Pullout capacity of plate anchor in sand by laboratory test[D]. Hefei: Hefei University of Technology, 2020.

[33] YAO Chen. Research on the vertical pull-out bearing characteristics of horizontal anchor plates in sand and the calculation method of bearing capacity[D]. Xiangtan: Hunan University of Science and Technology, 2021.

[34] ROWE R K, DAVIS E H. The behaviour of anchor plates in sand[J]. Géotechnique, 1982, 32(1): 25−41.

[35] State Grid Corporation of China. Q/GDW10584－2018 Technical regulation for design screw anchors foundation of overhead transmission line[S]. Beijing: China Electric Power Press, 2018.